THE JOURNAL OF PHYSICAL CHEMISTRY C

Subscriber access provided by NEW MEXICO STATE UNIV

C: Physical Processes in Nanomaterials and Nanostructures

Defect Evolution of Ion-Exposed Single-Wall Carbon Nanotubes

Jana Kalbacova, Elias Garratt, Raul D. Rodriguez, Angela R. Hight Walker, Kevin A. Twedt, Jeffrey A Fagan, Teresa I. Madeira, Jabez J. McClelland, Babak Nikoobakht, and Dietrich R. T. Zahn

J. Phys. Chem. C, **Just Accepted Manuscript** • DOI: 10.1021/acs.jpcc.8b08771 • Publication Date (Web): 03 Jan 2019

Defect Evolution of Ion-exposed Single-wall Carbon Nanotubes

Jana Kalbacova[†1,2], Elias Garratt[3], Raul D. Rodriguez[1,2,], Angela R. Hight Walker[4], Kevin A. Twedt[4,5], Jeffrey A. Fagan[6], Teresa. I. Madeira[1], Jabez J. McClelland[4], Babak Nikoobakht[3], Dietrich R.T. Zahn[1,2]*

[1]Semiconductor Physics, Technische Universität Chemnitz, 09107 Chemnitz, Germany

[2]Center for Advancing Electronics Dresden (cfaed), Technische Universität Chemnitz, 09107 Chemnitz, Germany

[3]Materials Measurement Science Division, National Institute of Standards and Technology, Gaithersburg, MD 20899, USA

[4]Physical Measurement Laboratory, National Institute of Standards and Technology (NIST), Gaithersburg, MD 20899, USA

[5]Maryland Nanocenter, University of Maryland, College Park, MD 20742, USA

[6]Materials Science and Engineering Division, National Institute of Standards and Technology, Gaithersburg, MD 20899, USA

*now at Tomsk Polytechnic University, 30 Lenin Ave, 634050 Tomsk, Russia

[†] Corresponding author. Tel: +49371 531-33999. E-mail: jana.kalbacova@physik.tu-chemnitz.de

ABSTRACT

The electronic properties of carbon nanotubes depend on several factors such as diameter, chirality, and defects. Defects such as vacancies can modify drastically the electronic properties of these nanostructures. The introduction of defects by irradiation processes cannot only lead to interesting defective nanomaterials but also tailor its intrinsic properties for specific electronic applications. The ability to accurately identify and quantify defects in carbon nanotubes is of major importance for their incorporation into electronic devices. We report on a newly developed quantitative method which combines a known fluence or pulse of ions from a focused beam source with Raman spectroscopy for characterization of defects enabling the detection of systematic variations in defect concentration emerging at 0.5% from different single-wall carbon nanotube types; semiconducting and metallic. It was also demonstrated that this result is independent from the selected ion species and its energy for thin films, which makes both types of ions suitable for these type of manipulations and characterization.

In this paper, the methods described and exploited can be performed without unique experimental setup or sample preparation and thus enable *in situ* accurate characterization of SWCNTs, devices, and other targeted applications.

1 INTRODUCTION

The electronic properties of ideal carbon nanotubes depend on their diameter and chirality[1]. However, carbon nanotubes are not as perfect as initially predicted by early theoretical works[2]. Even though single-wall carbon nanotube (SWCNT) sidewalls can be prepared without defects, for example, by chemical vapor deposition[3], the tube ends/caps can be still regarded as the defects intrinsic to SWCNTs[4], while other defects can be introduced by synthesis and processing methods[5]. Defects such as vacancies or dopants can drastically modify the electronic properties of these nanostructures[6].

Current state of the art for CNT fabrication is capable of producing single-wall carbon nanotubes (SWCNTs) of specific roll-types, *i.e.* diameters and chiralities[7]. On one hand, control over chiralities in production and further sorting has allowed researchers to study their electronic type, and led to some high profile applications, such as carbon nanotube field-effect transistors[8–10], on the other hand control over defects and their concentration is critical in obtaining reliable device function and lifetime[6]. In particular, due to the continuous miniaturization of devices, it is of utmost importance to be able to conduct defect studies, prospectively in their native environment, *i.e.* as incorporated in a device architecture.

Several approaches using *e.g.* fluorescence and nanoparticle labeling, and ion irradiation[11–17] were already reported and demonstrated an effective qualitative detection of the defect presence in SWCNTs created during synthesis or ion bombardment. However, a single methodology for defect quantification within a single SWCNT sample had not yet been established. Such methodology needs to be universally applicable while also enabling distinction between different SWCNT electronic types and chiralities.

Raman spectroscopy has a long history in the evaluation of SWCNT type and quality. One of the early applications was the determination of graphite crystallite size from two significant bands observed in the Raman spectrum, namely the D (disorder, ≈1350 cm^{-1}) and G (graphite, ≈1580 cm^{-1}) bands[18].

The D band corresponds to a hexagonal lattice breathing mode that is only Raman active if lattice distortions/defects are present. The direct contribution of the tube ends to the D band intensity was also shown in several tip-enhanced Raman spectroscopy studies[4,19] .

The shape of the G band originates from the tangential movement of the carbon atoms in SWCNTs and splits into two peaks G^- and G^+. At lower frequencies the G^- component of the band is chirality dependent and has a Lorentzian line shape for semiconducting SWCNTs and a Breit-Wigner-Fano line shape for metallic SWCNTs[20], while the more intense G^+ component of the band can be described by a Lorentzian function for both SWCNT electronic types. It was demonstrated by early measurements and studies[21] that this property can be used very effectively to differentiate between the two electronic-type SWCNTs,

metallic and semiconducting, or identify a minority sample component by choosing the laser excitation that matches SWCNT particular resonant conditions. Explanation on the resonance effect in carbon nanotubes can be found in the Supporting Information.

These aforementioned effects are the key to obtaining an accurate evaluation of the two electronic types of SWCNTs by Raman spectroscopy[21–23]. Nevertheless, to obtain a precise measure of the defect quantity, a quantitative technique is required. The combination of ion beam irradiation and Raman spectroscopy of the D to G peak intensity ratio (I_D/I_G) was already employed to quantify defects, average distance between defects, and their nature in graphene, few-layer graphene, and graphite[24–26].

The ability of ion irradiation to introduce defects relies on the simple mechanism of collisional displacement (knock-on) or pure energy deposition within SWCNTs (a non-ionizing energy loss mechanism) by the ion beam, misplacing carbon atoms out of the lattice positions. It is therefore a well-suited technique to introduce point-like defects. Given these factors, focused ion beam irradiation can be employed to evaluate the complete defect evolution within a single sample because it is capable of introducing defects down to single ion exposure[27], resulting in few point like vacancies within SWCNTs as well as controlling the spatial distribution of these defects.

In our work we explore the evolution of defects within SWCNTs thin films by controlling the spatial distribution and quantity of defects using light and heavy ion focused beams combined with different laser lines employed and matched to optical transitions of the most semiconducting or metallic SWCNTs. In comparison to previous works that only employed one laser line and hence were focusing only on a section of the SWCNT mixture[14,28], we show that by choosing the appropriate laser lines larger portions of the SWCNTs species can be studied. Moreover, we show that our method is independent of the choice of the ion beam. This offers a clear path towards the creation of areas of localized defects within devices like SWCNT transistors and when coupled with Raman spectroscopy provides a highly robust methodology to evaluate defect concentration that further affects device performance, reliability, and lifetime.

2 MATERIALS AND METHODS

Nanometer sized thin SWCNT films were prepared from sorted dispersions containing either primarily semiconducting or metallic SWCNTs[29,30] and further will be referred to as semiconducting 'sc' and metallic 'm' samples, respectively.

2.1 CARBON NANOTUBES PREPARATION

The semiconducting SWCNTs were produced by arc-discharge method by Carbon Solutions, Inc. giving an average diameter of ≈ (1.45 ± 0.1) nm and a length of about 450 nm as determined by atomic force microscopy **(**AFM)[31]. The metallic SWCNTs were produced via laser vaporization, which results in an average diameter of ≈ (1.35 ± 0.1) nm with a length of about 450 nm as determined by AFM[31–33]**.** The absolute enrichment of metallic *versus* semiconducting SWCNTs in such diameter distribution can be estimated using the procedure by Ding *et al.*[33] from visible-near infrared (vis-NIR) absorbance spectra in the wavelength range from 650 nm to 1200 nm and comparing against their best reported value (0.403) as 100% semiconducting purity. The spectra were collected using a Cary 5000 UV-vis-NIR through a quartz cuvette with the spectra of the blank surfactant solution collected separately and linearly subtracted during data analysis. For the semiconducting sample, the purity estimation methodology by Ding *et al.* yields (94 ± 1)%. The same procedure was also used to evaluate the metallic purity, however, the extracted value is more dependent on the fitting procedure and thus has a larger uncertainty. For this reason, the lower limit of the metallic purity was 91%.

2.2 CARBON NANOTUBE FILM PREPARATION

The SWCNT film was prepared *via* the vacuum filtration method and transferred to a silicon wafer with fiducial markers[34]. Briefly, a SWCNT dispersion volume to yield ≈ 10 nm film thickness (areal density ≈ 0.2 μg/cm^2) was filtered on a mixed cellulose ester (MCE) filter under vacuum. The resulting SWCNT film on the filter was cut onto smaller pieces (ca. 5 mm x 5 mm) and left overnight in ethanol. Then the filters

with SWCNTs were transferred face down onto the Si wafers and placed into acetone vapours for about an hour in order to dissolve the MCE filter. Finally, the samples were put into stirred acetone and methanol baths for 15 minutes each to remove any residual MCE filter. Samples prepared in such a way exhibit homogenous thickness, can be prepared on large areas, and are purified of any unwanted residues used in their preparation process.

2.3 FOCUSED ION BEAM IRRADIATION

Defects were induced in highly ordered pyrolytic graphite (HOPG) and the SWCNT films using focused ion beam irradiation from laser-cooled[35] and liquid metal ion sources generating beams of 4 keV Li^+ (in-house made[35,36]) and 30 keV Ga^+ (FEI Nova Nanolab) ions, respectively. All samples were exposed to the ion beam in doses from $3 \cdot 10^{10}$ ions/cm^2 to 10^{15} ions/cm^2 (5 orders of magnitude) in a patterned array consisting of 16 irradiated squares with size 5 µm x 5 µm each spaced 3 µm apart as sketched in Figure 1a. The fluence *per* irradiated square was controlled by regulating the exposure time of the beam at a constant current of 3.85 pA for Ga^+ and 0.8 pA for Li^+ within each irradiated square. To minimize errors in defect analysis, samples were otherwise blocked from electron imaging or focused ion beam exposure before and after generation of the defect arrays. With this procedure we expected to cover the defect evolution up to the amorphous carbon stage. For a detailed discussion of the method implementation please refer to SI.

2.4 CALCULATIONS

Transport of ions in matter (TRIM) simulations[37] were performed in order to determine and choose the optimal penetration depth of the ions, the depth vacancy distributions, and subsequently the number of created vacancies in the SWCNT films. Beam energies of 4 keV for Li^+ and 30 keV for Ga were chosen to create congruent penetration profiles and thus limit the variability of ion distributions despite Ga^+ projected to deliver a higher concentration of defects per unit volume *vs.* Li^+ owing to its significantly higher mass and energy (see Figure 1b, c). Further details on the ion beam irradiation as well as the recipe

for the calculations, and the artifacts produced by the calculation can be found in the Supporting Information.

Certain equipment, instruments, or materials are identified in this paper in order to adequately specify the experimental details. Such identification does not imply recommendation by the National Institute of Standards and Technology, nor does it imply the materials are necessarily the best available for the purpose.

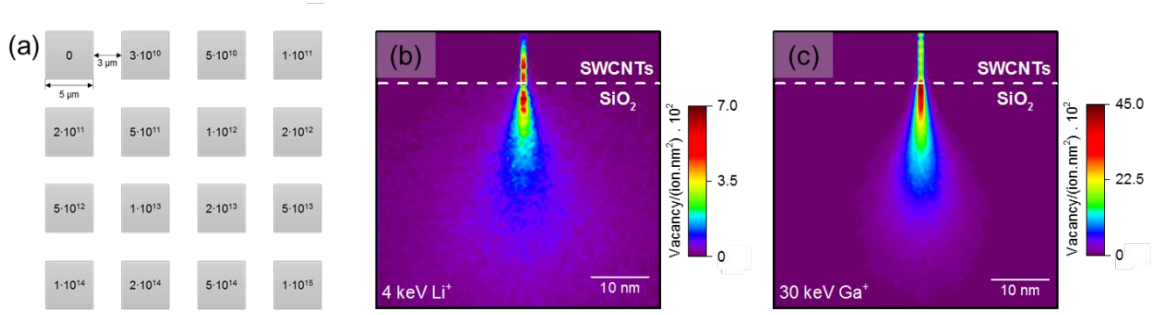

Figure 1. TRIM calculations of lithium (a) and gallium (b) ion generated depth vacancy map of irradiated 10 nm thick SWCNT films on a SiO_2 layer with a sketch of the ion bombardment pattern and fluence in ions/cm^2 (c).

2.5 CHARACTERIZATION

The samples were studied with two Raman spectrometers: 1. Renishaw inVia with the 514.5 nm laser line focused by a 100x long working distance objective (N.A. 0.7), 1800 l/mm grating; 2. Horiba LabRam HR800 with the 514.7 nm and 632.8 nm laser lines focused by 100x objective (N.A. 0.9), 600 l/mm grating and liquid nitrogen cooled CCD. The total power used at the sample was set below 1 mW to avoid creation of further defects or local heating. The Raman imaging maps were generated for 35 µm x 35 µm large areas with a step size of 0.5 µm. So far, the most commonly used method to evaluate defects is the intensity (*i.e.* the peak maxima) ratio of D to G$^+$ bands[24] providing a comparative measure of defects (here I_D/I_{G+}).

The Kataura plot was used to identify which SWCNT is resonant with certain laser excitation or *vice versa*, which laser line is suitable for a specific electronic type or chirality. More details can be found in the Supporting Information. Even though non-resonant transitions are also present, compared to the resonant contribution, which is much larger, the signal from an isolated SWCNT can be expected in an energy window of maximum 0.2 eV.

3 RESULTS AND DISCUSSION

For graphite, the ion induced damage was classified in several stages - from graphite covering nano-crystalline and amorphous graphite stages to tetrahedral amorphous carbon[24,38]. In order to have a comparison of the ion irradiation process on the SWCNTs, the same experiment was performed on highly ordered pyrolytic graphite (HOPG) as a reference with known behaviour[39,40] and the results can be found in the Supporting Information. Shortly, the Raman spectroscopy measurements are in agreement with previous reports[39,40].

In Figure 2a, b Raman spectra of pristine and ion irradiated (defected) SWCNT films are shown for two different excitation wavelengths. The first laser excitation used, 514.5 nm (2.41 eV) is in resonance with semiconducting SWCNTs, while the second, 632.8 nm (1.96 eV) laser line, is in resonance with metallic SWCNTs (see UV-vis-NIR absorbance spectra in Figure 2c). This means that with the 514.5 nm line mostly the semiconducting carbon nanotubes are resonant, *i.e.* they are observed with this excitation energy independent of whether the sample has semiconducting SWCNT as a majority or a minority component. For the 632.8 nm line the situation is inverted and thus mostly the metallic SWCNT show up in the Raman spectra. As a confirmation of the two electronic types coexisting in the sample, we can see the different line shapes of the G^- band taken under different resonance conditions and furthermore that they retain their initial nature after ion irradiation.

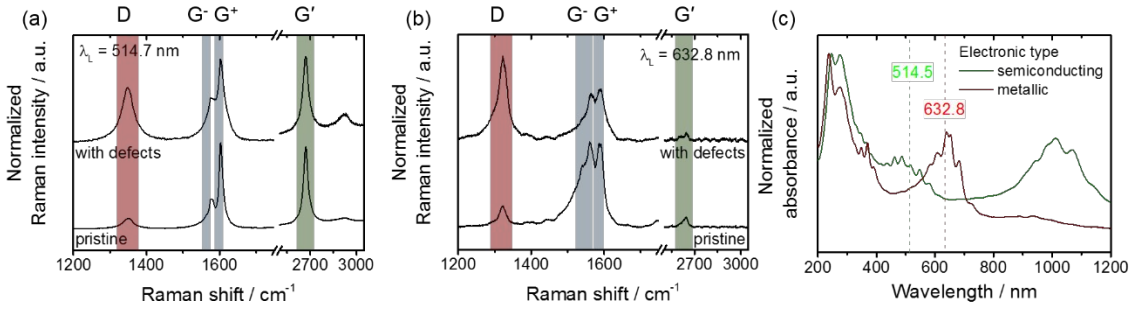

Figure 2. Comparison of pristine and irradiated metallic (at fluence of 10^{13} ions/cm^2) SWCNTs under laser excitation of 514.5 nm (a) and 632.8 nm (b), and the UV-vis-NIR absorbance spectra for pristine samples (c) showing the position of laser lines employed in the Raman spectroscopy investigation as dashed lines.

From the experimental results, we observe that at first, with increasing ion bombardment dose, the D band intensity rises, while the G^+ band intensity stays constant and thus I_D/I_{G+} increases (see also Figure 3).

However, with higher doses the absolute intensities of both the D and G^+ bands decrease due to a sputtering effect of the focused ion beam causing a loss of sp^2 hybridized carbon atoms and/or the structural breakdown. With further increase of the ion dose the defect concentration saturates. In the last stage, the D and G^+ band intensities decrease further as well as the I_D/I_G+ ratio. Here, the SWCNTs become amorphized exhibiting two wide bands at 1350 cm^{-1} and 1600 cm^{-1} that have much lower intensity when compared to the original signal of pristine SWCNTs. In addition, with increasing irradiation dose the radial breathing mode (RBM) changes. This mode is highly sensitive to environmental changes and also has a smaller resonance window, *i.e.* fewer SWCNT chiralities are in resonance and contribute to the Raman scattering, which allows a smaller number of SWCNT chiralities to be probed compared to other modes such as the G band[41]. We observe that the onset of RBM intensity decrease is similar to the onset of decrease of the G^+ band (see Figure S3 in Supporting Information). An elaborate discussion the RBM behavior is beyond the scope of this paper and will be published elsewhere.

Figure 3 shows the Raman spectroscopy results for both metallic and semiconducting SWCNT films after Li^+ ion and Ga^+ ion bombardment at several doses. The displayed spectra were averaged over several

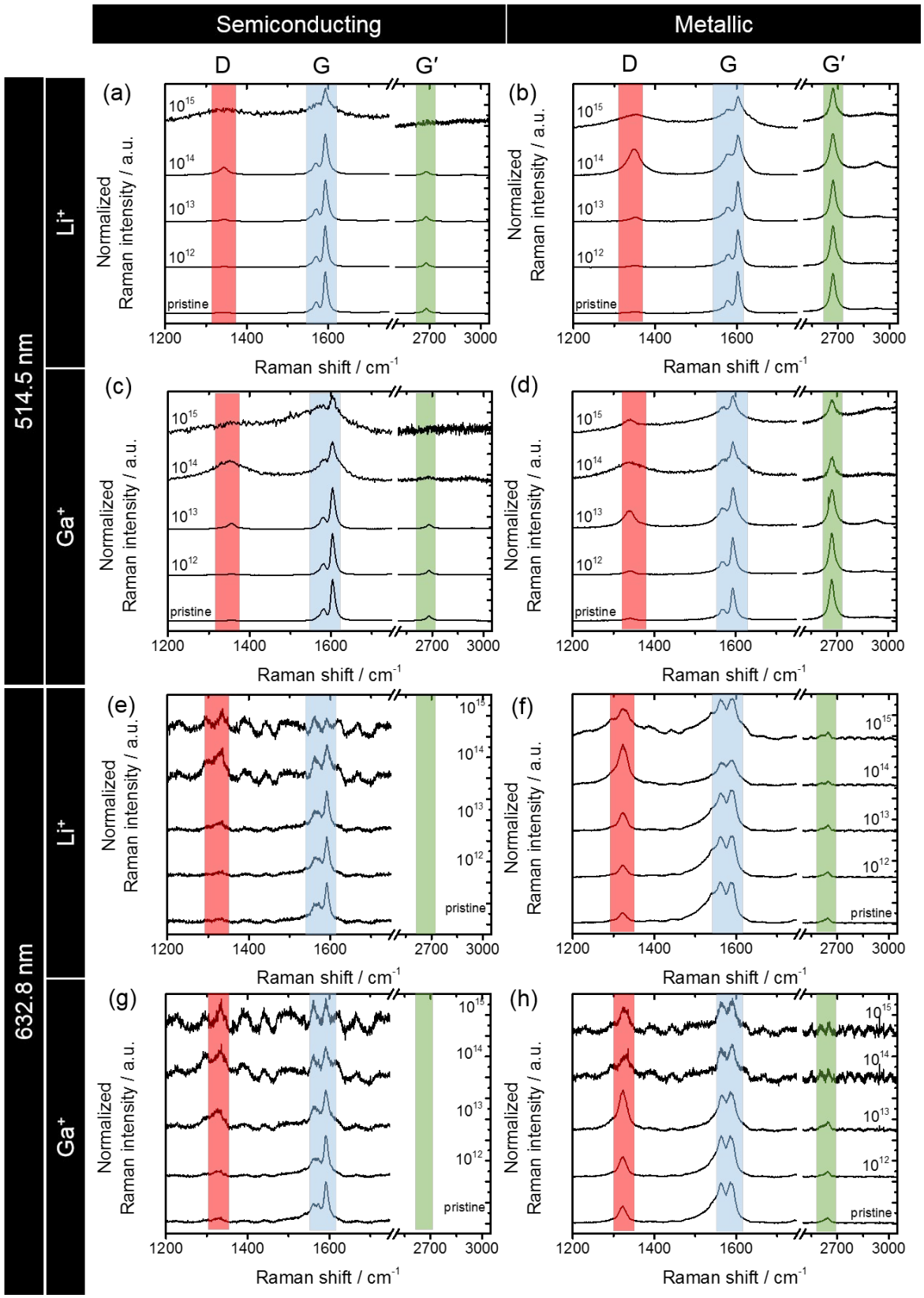
Semiconducting
Metallic
D
G
G′
514.5 nm
632.8 nm
Li+
Ga+
(a)
(b)
(c)
(d)
(e)
(f)
(g)
(h)
Normalized Raman intensity / a.u.
Raman shift / cm-1
10^15
10^14
10^13
10^12
pristine
1200
1400
1600
2700
3000

Figure 3. Comparison of Raman spectra of semiconducting and metallic SWCNTs bombarded with Li^+ (a, b, e, f) and Ga^+ (c, d, g, h) ions measured with 514.5 nm (a-d) and 632.8 nm (e-h) laser lines under different irradiation doses. These spectra are the result of more than 25 averaged spectra from different points within the dosed area. In (e, g) the G' band region was not recorded due to the very poor signal-to-noise ratio.

measurements points (> 25) in the middle of the respective irradiated region within the pattern. Even though the I_D/I_{G+} ratio is considered as the standard for the evaluation of defect concentration, other ratios should be taken into account as well. One such intensity ratio is that of the G' band to the D band. The G' band is found near 2650 cm^{-1} (also called 2D band[42]) and originates from two-phonon scattering. Contrary to the D band, the G' does not require defects for activation. Qualitatively comparing the two intensity ratios I_D/I_{G+} and $I_D/I_{G'}$, we observe similar trends with irradiated dose. The onsets of the $I_D/I_{G'}$ increase as well as the maxima of the intensity ratios remain at the same positions. However, due to the fact that the $I_D/I_{G'}$ values have a higher absolute magnitude in comparison to I_D/I_{G+} we can regard it as a more sensitive measure of smaller changes[14]. On the other hand, from the instrumental point of view, the large frequency difference between D and G' bands limits their simultaneous acquisition (especially when high spectral resolution is required).

Contrary to graphene that can be prepared nearly without defects, *e.g.* by mechanical exfoliation, SWCNTs possess an intrinsic defect concentration as deduced from the non-irradiated (pristine) area of Raman maps (see Figure 4). For example, the I_D/I_G+ of the semiconducting sample is 0.028 ± 0.002 when measured with the 514.5 nm excitation line. These defects present in the pristine sample are related to tube ends[4,19] and/or structural defects from the sample preparation procedure[5]. These effects can be observed in Figure 4, where the semiconducting sample has lower I_D/I_{G+} ratio compared to the metal-SWCNT rich sample. The Raman mapping also shows a small variability in I_D/I_{G+} consistent with the topographical features and correlated with the sample thickness by atomic force microscopy (AFM), *i.e.* thinner areas have slightly higher I_D/I_{G+} compared to thicker areas (see Figure S4 in Supporting

Information). This effect was already investigated and explained by increased substrate interaction[43] and also by increased oxygen exposure of the SWCNTs[44,45].

As was already experimentally observed in the work by Pollard *et al.*[46], the ion size plays an important role in the amount of sample damage for the same ion dose. The TRIM simulation results (in Figure 1b, c) show that the total number of vacancies in the SWCNT layer created by Ga^+ ions should be 4.8 times higher than by Li^+ ions of the same fluence. This tendency is also experimentally observed, *i.e.* the I_D/I_{G+} ratios of the samples (Figure 4a, c and Figure 4b, d) differ for the same ion doses. For example, the defect concentration introduced by Li^+ ions at $2 \cdot 10^{14}$ ions/cm^2 dose is comparable to a dose of Ga^+ $1 \cdot 10^{13}$ ions/cm^2.

Another notable result is how defects are not contained or homogeneously distributed beyond and within the expected, *i.e.* nominally dosed, area of the 5 µm x 5 µm square. The most probable causes of this effect are due to the beam spread[47] and enhanced damage production due to overlapping characteristic

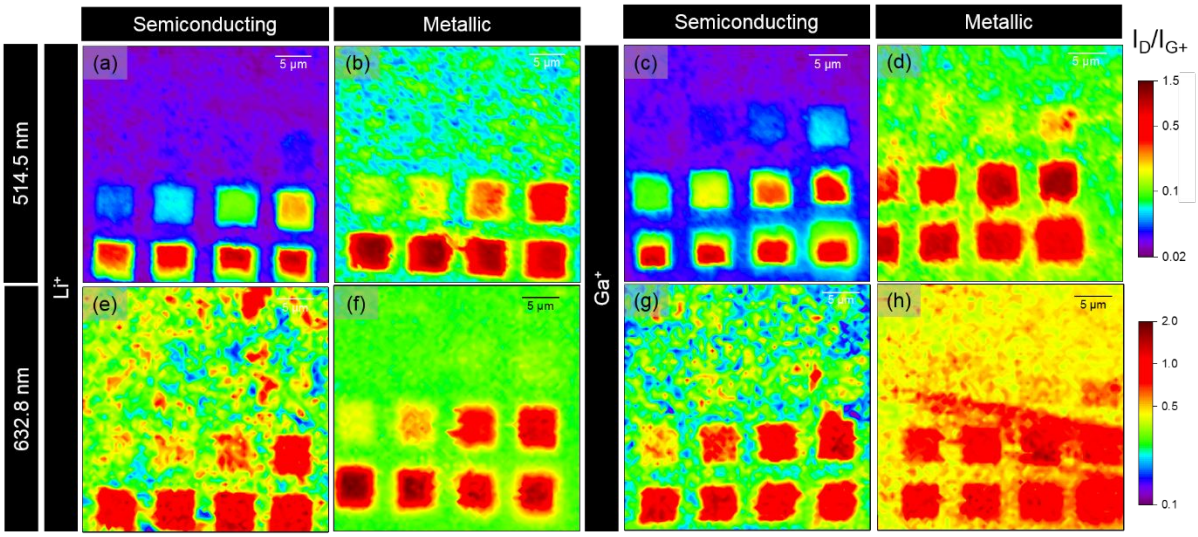

Figure 4. Comparison of I_D/I_{G+} ratios of semiconducting and metallic SWCNTs bombarded with Li^+ and Ga^+ ions measured with 514.5 nm (a-d) and 632.8 nm (e-h) laser lines. For clarity data in one line are plotted with common color bar.

diffusion lengths of damage cascades. The result is contributing to local heating and thus higher defect mobility introduced by the intense irradiation at higher doses[26,47–49]. The Li^+ focused ion beam is expected to have a Gaussian distribution, however, the tails of the distribution are not precisely known. To quantify the topography of the irradiated surfaces and visualize the extent of the irradiated region and the border sharpness of the unirradiated (pristine) and irradiated region, we performed AFM and Raman experiments on graphite with the same irradiation pattern and doses as for the SWCNT samples (see the previous section). The AFM results for the higher dose of Ga^+ ions on graphite show a *ca.* 100 nm interface region at high fluence. The irradiated/pristine border sharpness can be also attributed to the diffraction-limited spatial resolution of *ca.* 1 µm of the Raman microscope. Owing to the precision of the focused ion beam, a direct comparison of the irradiation effect on the SWCNT structure for Li^+ ions is possible. We can conclude that in low dose cases (below $1{\cdot}10^{14}$ ions/cm^2) the microscale structure of SWCNT remains intact and the smearing effect of the irradiated/pristine border in the I_D/I_{G+} ratio is likely connected to the Raman measurement. In higher dose cases effects of overlapping characteristic diffusion lengths of damage cascades is a likely contribution to smearing effects of the I_D/I_{G+} ratio.

Figure 5 summarises the results for semiconducting and metallic SWCNT samples irradiated with both Ga^+ and Li^+ ions and measured with the two different laser lines. There is a notable difference between the value of the I_D/I_{G+} ratio of pristine semiconducting and metallic samples with 514.5 nm excitation wavelength (0.028 ± 0.002 *vs*. 0.074 ± 0.016, respectively) and they exhibit contrasting behaviour upon irradiation with the same ion doses. Additionaly, even though the onset of observable change in I_D/I_{G+} ratio upon ion irradiation of the metallic SWCNTs is comparable to the semiconducting SWCNTs, their absolute I_D/I_{G+} ratios are significantly higher.

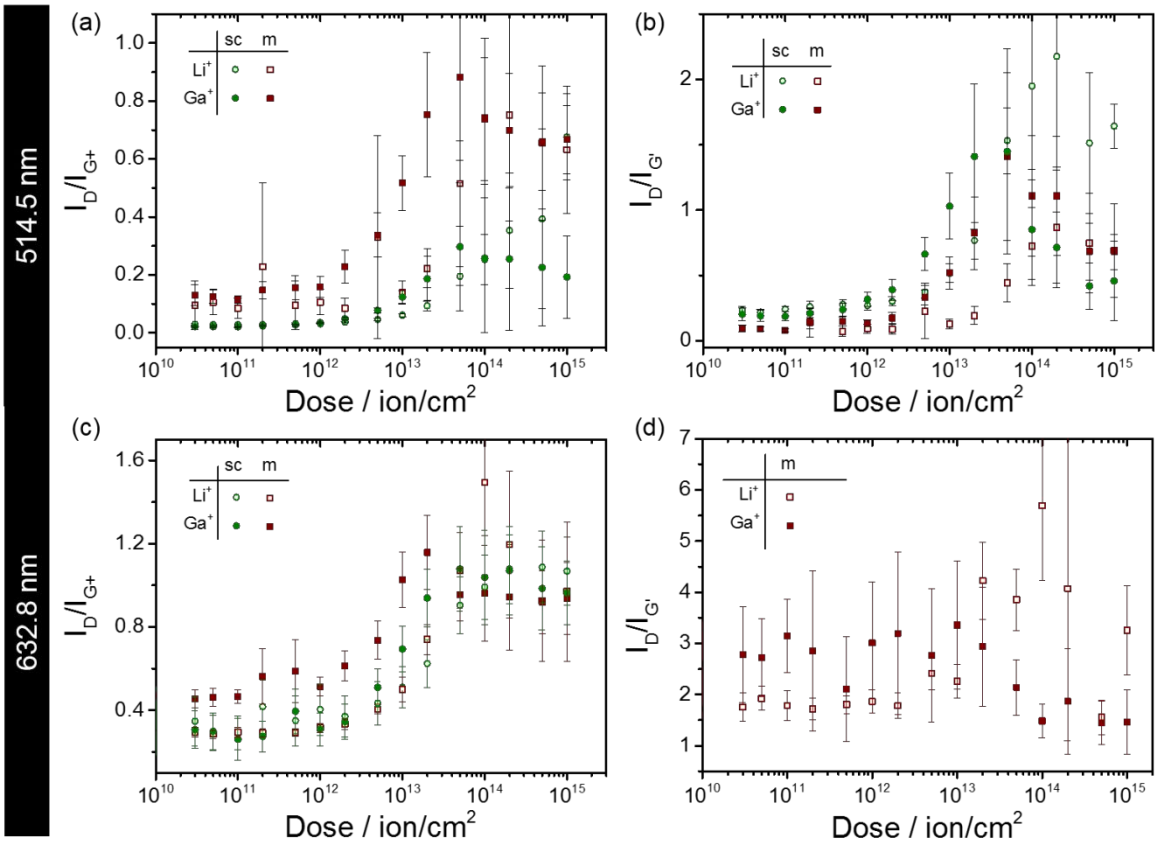

Figure 5. Comparison of I_D/I_{G+} (a, c) and $I_D/I_{G'}$ (b, d) ratios for semiconducting and metallic SWCNTs bombarded with Li^+ and Ga^+ ions as measured with 514.5 nm (a, b) and 632.8 nm (c, d) laser lines. The average values for each dose were evaluated solely within the 5 µm x 5 µm irradiated patterns.

Raman data collected with 514.5 nm excitation probe more semiconducting nanotubes, while those collected with 632.8 nm excitation probe more metallic tubes due to the resonance conditions discussed above (valid for our diameter range, see UV-vis-NIR absorption spectra in Figure 2c). The important point here is that since more semiconducting nanotubes are in resonance, they make a larger contribution to the Raman spectra with the 514.5 nm laser line. Under 632.8 nm excitation the metallic SWCNTs are more resonant and the situation inverts. For this reason, it is important to notice that a direct comparison between semiconducting and metallic samples, particularly of the same diameter distribution, under only one laser excitation is generally impractical and is likely to be inaccurate. In the case of the 514.5 nm laser

and semiconducting samples, the G band arises from the majority of the SWCNTs present, whereas in the metallic sample the semiconducting SWCNTs probed are in the minority.

It is also important to notice that comparing intensity ratios alone does not give complete information on the different types of defects present. Some of the defects, such as charged impurities, strain, or intercalants do contribute to D band intensity[24]. In addition, doping was demonstrated to have an effect on the I_D/I_G intensity ratio in graphene[42] and in SWCNTs[50]. However, shifts in G and G' band positions also occur if the doping level changes. Such systematic peak position shifts were not observed in our results and thus we infer that doping of the SWCNT layer due to ion irradiation is negligible. The process of defect generation within SWCNT films using ion irradiation is through primary knock-on and secondary recoils of ions in the non-ionizing regime. In order to be able to compare the effects of different ions, consecutive simulations in TRIM[37] were employed to account for the different ion sizes and energies. In this way, the created vacancies can be spectroscopically investigated and compared to the Raman I_D/I_{G+} ratios from the same area. As previously described in literature[14,51], the number of vacancies created upon ion impact and by recoil calculated in TRIM (SWCNT density 0.5 g/cm^3; displacement threshold energy 19 eV) is converted into the non-ionizing energy loss (NIEL). NIEL values strongly depend on the scattering cross section and vary greatly between 4 keV Li^+ and 30 keV Ga^+, however, in the < 10 nm SWCNT films the relative variation in NIEL values for each ion is low. Therefore, an average NIEL value, $NIEL_{eff}$ for each ion species was employed. This value for each ($NIEL_{eff}$ (Li^+) = 363.19 MeV/g, $NIEL_{eff}$ (Ga^+) = 2291.66 MeV/g) is then multiplied by the ion fluence to obtain the displacement damage dose (DDD, DDD = $NIEL_{eff}$*fluence), which is directly proportional to the density of vacancies. In Figure 6 the normalized I_D/I_{G+} ratios (divided by the I_D/I_{G+} ratio of the pristine SWCNT film) are plotted against the defect concentration (c_D), calculated as:

$$c_D = DDD \cdot \frac{m_c \cdot N_A}{E_{vac}} \cdot 100\ [\%],$$

where E_{vac} is the energy required to produce a vacancy (50.5 eV[28,52]), m_c is the atomic weight of carbon, N_A is Avogadro's number. A value of c_D greater than 100% means that there is a higher number of

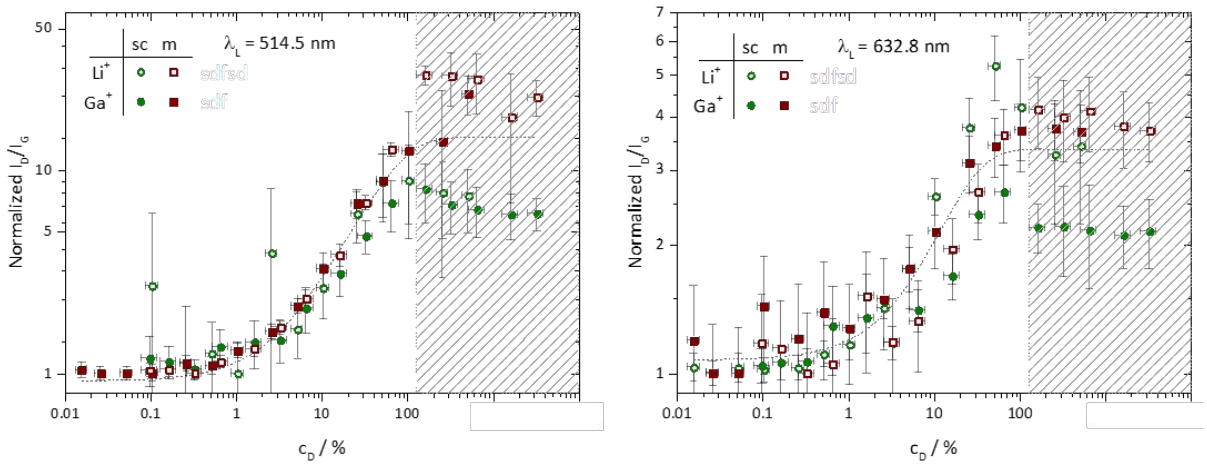

Figure 6. Normalized I_D/I_{G+} (divided by the I_D/I_{G+} ratio of the pristine SWCNT film) plotted against calculated defect concentration (c_D) of the SWCNT upon ion irradiation for the 514.5 nm (a) and 632.8 nm (b) laser lines. The dashed lines represent a guide for the eye. The shaded area indicates the region above the nominal 100% of defect concentration, *i.e.* the number of defects is greater than the number of carbon atoms.

defects/vacancies than carbon atoms, in other words, the total number of defects exceeds the total number of carbon atoms. Therefore, an amorphous carbon structure is formed as is confirmed by the plateau in the normalized I_D/I_{G+} ratio. This behavior was already reported for graphite[39,53]. The presence of amorphous carbon is also confirmed by the Raman spectra itself, *i.e.* by its broad D and G peaks and the absence of the G' band.

From these data in the Figure 6 we can see the emergence of a systematic exponential increase in the I_D/I_{G+} ratio is identifiable from defect concentrations as small as 0.5%, *i.e.* one defect/vacancy *per* 200 carbon atoms. This systematic increase is distinguishable along the x-axis but not along the y-axis. Here, it is possible to detect up to 2% with 514.5 nm laser excitation and about 5% with 632.8 nm laser as a lower limit for defect detection. For a systematic error calculation please refer to the Supporting

Information section. Interestingly, although the $NIEL_{eff}$ values for 30 keV Ga^+ ions are larger than those of Li^+ by a factor of ≈ 5 they follow the same I_D/I_{G+} curve. This implies that it is possible to obtain an accurate measurement of the defect concentration regardless of the beam species for thin samples as long as their chemical structure and thickness are similar, as both types of ions primarily induce defects via the same physical mechanism, NIEL, vs. knock-on collisions. Detailed explanation and step-by-step guide to reproduce the results was included into SI.

To illustrate the effective defect/vacancy separation in a single SWCNT, we chose a tube with (10,10) chirality (d_t = 1.36 nm; 163 atoms/nm = $N_{T/nm}$), which is present in the SWCNT samples as demonstrated by its absorbance around 640 nm (see Figure 2c). Here, the selection of chirality is not as important as the tube diameter and the corresponding number of atoms per tube length. The effective defect/vacancy distance is calculated as:

$$L_{eff} = \frac{10^2}{c_D \cdot N_{T/nm}}$$ This means that for defect concentration of 1% in such (10,10) nanotube the defects deduced from the Raman spectra will be spaced less than 1 nm apart. The distance of defects is a size dependent effect, the smaller the tube diameter is, for the same ion fluence, the wider is the spacing between defects along the length of the tube[51]. However, from scanning tunneling microscopy observations of ion irradiated graphene[46,53], we know that one ion creates more than one defect in the profile/beam cross section area and thus we can assume that this defect site distance in pristine SWCNT is larger than 1 nm.

4 CONCLUSIONS

This paper presents the results of a systematic evaluation and quantification of defects in electronic type sorted SWCNTs, highly enriched semiconducting and metallic, and provides a versatile and accessible tool for characterization of SWCNTs.

As proper sample preparation is essential for all kind of experiments a protocol was established for obtaining surfactant and residue free SWCNT films with the possibility to adjust to a desired film thickness. Such films were employed in the in-depth investigation of SWCNT defects. This was achieved by controlled bombardment of the samples with different focused ion beams. Two electronic types of SWCNTs – semiconducting and metallic – were studied with two excitation laser lines, *i.e.* under the respective resonance conditions. The intensity ratios of the Raman bands were used to monitor the evolution of defects with increasing irradiation dose. Here, Raman spectroscopy was found to be sensitive to defect concentrations as low as 0.5%, independent from the selected ion species and its energy. With the known doses of ions, the defect quantification becomes available as a tool in the SWCNT quality analysis. Furthermore, focused ion irradiation with light (Li^+) and heavy (Ga^+) ions confirmed the viability of both ion types to perform an accurate quantification study of defects. The methods described and exploited can be performed without unique experimental setup or sample preparation enabling accurate *in situ* characterization of SWCNT, its devices, and other targeted applications.

ACKNOWLEDGEMENTS

This work was funded by the German Research Foundation (DFG) within the Cluster of Excellence “Center for Advancing Electronics Dresden” (cfaed) and the Research Unit FOR1713 "Sensoric Micro- and Nanosystems“. R.D.R. also acknowledges TPU Competitiveness Enhancement Program. This work was performed in the context of the European COST Action MP1302 Nanospectroscopy. K.A.T. acknowledges support under the Cooperative Research Agreement between the University of Maryland and the National Institute of Standards and Technology Center for Nanoscale Science and Technology, Award 70NANB10H193, through the University of Maryland.

Authors would like to thank Cory D. Cress for the valuable discussion on the vacancy analysis and Maximilian Männig for help with data processing.

SUPPORTING INFORMATION

Supporting Information Available: Contains additional information on Radiation-solid Interaction Effects and Ion Bombardment Conditions, Method Implementation with detailed step-by-step guide, results on graphite reference sample, results on Raman measurements of SWCNTs radial breathing mode, and explanation of resonance effect and Kataura plot for SWCNTs. Full calculation is available with xls data sheet. This material is available free of charge via the Internet at http://pubs.acs.org.

REFERENCES

(1) Iijima, S. Helical Microtubules of Graphitic Carbon. *Lett. to Nat.* **1991**, *354*, 56–58.

(2) Krasheninnikov, A. V.; Lehtinen, P. O.; Foster, A. S.; Nieminen, R. M. Bending the Rules: Contrasting Vacancy Energetics and Migration in Graphite and Carbon Nanotubes. *Chem. Phys. Lett.* **2006**, *418*, 132–136.

(3) Shadmi, N.; Kremen, A.; Frenkel, Y.; Lapin, Z. J.; Machado, L. D.; Legoas, S. B.; Bitton, O.; Rechav, K.; Popovitz-Biro, R.; Galvão, D. S.; et al. Defect-Free Carbon Nanotube Coils. *Nano Lett.* **2016**, *16*, 2152–2158.

(4) Liao, M.; Jiang, S.; Hu, C.; Zhang, R.; Kuang, Y.; Zhu, J.; Zhang, Y.; Dong, Z. Tip-Enhanced Raman Spectroscopic Imaging of Individual Carbon Nanotubes with Subnanometer Resolution. *Nano Lett.* **2016**, *16*, 4040–4046.

(5) Kim, U. J.; Furtado, C. a.; Liu, X.; Chen, G.; Eklund, P. C. Raman and IR Spectroscopy of Chemically Processed Single-Walled Carbon Nanotubes. *J. Am. Chem. Soc.* **2005**, *127*, 15437–15445.

(6) Neophytou, N.; Kienle, D.; Polizzi, E.; Anantram, M. P. Influence of Defects on Nanotube Transistor Performance. *Appl. Phys. Lett.* **2006**, *88*, 24–27.

(7) Ibrahim, I.; Kalbacova, J.; Engemaier, V.; Pang, J.; Rodriguez, R. D.; Grimm, D.; Gemming, T.; Zahn,

D. R. T.; Schmidt, O. G.; Eckert, J.; et al. Confirming the Dual Role of Etchants during the Enrichment of Semiconducting Single Wall Carbon Nanotubes by Chemical Vapor Deposition. *Chem. Mater.* **2015**, *27*, 5964–5973.

(8) Martel, R.; Schmidt, T.; Shea, H. R.; Hertel, T.; Avouris, P. Single- and Multi-Wall Carbon Nanotube Field-Effect Transistors. *Appl. Phys. Lett.* **1998**, *73*, 2447–2449.

(9) Tans, S.; Verschueren, A.; Dekker, C. Room-Temperature Transistor Based on a Single Carbon Nanotube. *Nature* **1998**, *672*, 669–672.

(10) Rodriguez, R. D.; Toader, M.; Hermann, S.; Sheremet, E.; Müller, S.; Gordan, O. D.; Yu, H.; Schulz, S. E.; Hietschold, M.; Zahn, D. R. Nanoscale Optical and Electrical Characterization of Horizontally Aligned Single-Walled Carbon Nanotubes. *Nanoscale Res. Lett.* **2012**, *7*, 682–688.

(11) Dementev, N.; Feng, X.; Borguet, E. Fluorescence Labeling and Quantification of Oxygen-Containing Functionalities on the Surface of Single-Walled Carbon Nanotubes. *Langmuir* **2009**, *25*, 7573–7577.

(12) Fan, Y.; Burghard, M.; Kern, K. Chemical Defect Decoration of Carbon Nanotubes. *Adv. Mater.* **2002**, *14*, 130–133.

(13) Fan, Y.; Goldsmith, B. R.; Collins, P. G. Identifying and Counting Point Defects in Carbon Nanotubes. *Nat. Mater.* **2005**, *4*, 906–911.

(14) Rossi, J. E.; Cress, C. D.; Helenic, A. R.; Schauerman, C. M.; Dileo, R. A.; Cox, N. D.; Messenger, S. R.; Weaver, B. D.; Hubbard, S. M.; Landi, B. J. Ion Irradiation of Electronic-Type-Separated Single Wall Carbon Nanotubes : A Model for Radiation Effects in Nanostructured Carbon. *J. Appl. Phys.* **2012**, *034314*, 1–11.

(15) Adhikari, A. R.; Huang, M.; Bakhru, H.; Vajtai, R.; Ryu, C. Y.; Ajayan, P. M. Stability of Ion Implanted Single-Walled Carbon Nanotubes: Thermogravimetric and Raman Analysis. *J. Appl. Phys.* **2006**, *100*, 0–5.

(16) Jeet, K.; Jindal, V. K.; Bharadwaj, L. M.; Dharamvir, K. Structural Modification of Single Wall and Multiwalled Carbon Nanotubes under Carbon, Nickel and Gold Ion Beam Irradiation. *Int. Conf. Adv. Condens. Nano Mater.* **2011**, *1393*, 67–68.

(17) Skákalová, V.; Woo, Y.-S.; Osváth, Z.; Biró, L. P.; Roth, S. Electron Transport in Ar^+-Irradiated Single Wall Carbon Nanotubes. *Phys. Status Solidi* **2006**, *243*, 3346–3350.

(18) Tuinstra, F.; Koenig, L. Raman Spectrum of Graphite. *J. Chem. Phys.* **1970**, *53*, 1126–1130.

(19) Chen, C.; Hayazawa, N.; Kawata, S. A 1.7nm Resolution Chemical Analysis of Carbon Nanotubes by Tip-Enhanced Raman Imaging in the Ambient. *Nat. Commun.* **2014**, *5*, 3312.

(20) Telg, H.; Duque, J. G.; Staiger, M.; Tu, X.; Hennrich, F.; Kappes, M. M.; Zheng, M.; Maultzsch, J.; Thomsen, C.; Doorn, S. K. Chiral Index Dependence of the G+ and G- Raman Modes in Semiconducting Carbon Nanotubes. *ACS Nano* **2012**, *6*, 904–911.

(21) Rao, A. M.; Richter, E.; Bandow, S.; Chase, B.; Eklund, P. C.; Williams, K. A.; Fang, S.; Subbaswamy, K. R.; Menon, M.; Thess, A.; et al. Diameter-Selective Raman Scattering from Vibrational Modes in Carbon Nanotubes. *Science* **1997**, *275*, 187–191.

(22) Kataura, H.; Kumazawa, Y.; Maniwa, Y.; Umezu, I.; Suzuki, S.; Ohtsuka, Y.; Achiba, Y. Optical Properties of Single-Wall Carbon Nanotubes. *Synth. Met.* **1999**, *103*, 2555–2558.

(23) Jorio, A.; Souza Filho, A.; Dresselhaus, G.; Dresselhaus, M.; Swan, A.; Ünlü, M.; Goldberg, B.; Pimenta, M.; Hafner, J.; Lieber, C.; et al. G-Band Resonant Raman Study of 62 Isolated Single-Wall Carbon Nanotubes. *Phys. Rev. B* **2002**, *65*, 23–27.

(24) Cançado, L. G.; Jorio, A.; Ferreira, E. . H. M.; Stavale, F.; Achete, C. A.; Capaz, R. B.; Moutinho, M. V. O.; Lombardo, A.; Kulmala, T. S.; Ferrari, A. C. Quantifying Defects in Graphene via Raman Spectroscopy at Different Excitation Energies. *Nano Lett.* **2011**, *11*, 3190–3196.

(25) Eckmann, A.; Felten, A.; Mishchenko, A.; Britnell, L.; Krupke, R.; Novoselov, K. S.; Casiraghi, C. Probing the Nature of Defects in Graphene by Raman Spectroscopy. *Nano Lett.* **2012**, *12*, 3925–

3930.

(26) Liao, Z.; Zhang, T.; Gall, M.; Dianat, A.; Rosenkranz, R.; Jordan, R. Lateral Damage in Graphene Carved by High Energy Focused Gallium Ion Beams Lateral Damage in Graphene Carved by High Energy Focused Gallium Ion Beams. *Appl. Phys. Lett.* **2015**, *107*, 0131081–0131086.

(27) Singh, M.; Pacheco, J. L.; Perry, D.; Garratt, E.; Ten Eyck, G.; Bishop, N. C.; Wendt, J. R.; Manginell, R. P.; Dominguez, J.; Pluym, T.; et al. Electrostatically Defined Silicon Quantum Dots with Counted Antimony Donor Implants. *Appl. Phys. Lett.* **2016**, *108*, 0–4.

(28) Merrill, A.; Cress, C. D.; Rossi, J. E.; Cox, N. D.; Landi, B. J. Threshold Displacement Energies in Graphene and Single-Walled Carbon Nanotubes. *Phys. Rev. B* **2015**, *92*, 075404.

(29) Khripin, C. Y.; Fagan, J. A.; Zheng, M. Spontaneous Partition of Carbon Nanotubes in Polymer-Modified Aqueous Phases. *J. Am. Chem. Soc.* **2013**, *135*, 6822–6825.

(30) Gui, H.; Streit, J. K.; Fagan, J. A.; Hight Walker, A. R.; Zhou, C.; Zheng, M. Redox Sorting of Carbon Nanotubes. *Nano Lett.* **2015**, *15*, 1642–1646.

(31) Fagan, J. A.; Haroz, E. H.; Ihly, R.; Gui, H.; Blackburn, J. L.; Simpson, J. R.; Lam, S.; Walker, A. R. H.; Doorn, S. K.; Zheng, M. Isolation of > 1nm Diameter Single-Wall Carbon Nanotube Species Using Aqueous Two-Phase Extraction. *ACS Nano* **2015**, *9*, 5377–5390.

(32) Mistry, K. S.; Larsen, B. A.; Blackburn, J. L. High-Yield Dispersions of Large-Diameter Semiconducting Single-Walled Carbon Nanotubes with Tunable Narrow Chirality Distributions. *ACS Nano* **2013**, *7*, 2231–2239.

(33) Ding, J.; Li, Z.; Lefebvre, J.; Cheng, F.; Dubey, G.; Zou, S.; Finnie, P.; Hrdina, A.; Scoles, L.; Lopinski, G. P.; et al. Enrichment of Large-Diameter Semiconducting SWCNTs by Poly Fluorene Extraction for High Network Density Thin Film Transistors. *Nanoscale* **2014**, *6*, 2328–2339.

(34) Wu, Z.; Chen, Z.; Du, X.; Logan, J. M.; Sippel, J.; Nikolou, M.; Kamaras, K.; Reynolds, J. R.; Tanner, D. B.; Hebard, A. F.; et al. Transparent, Conductive Carbon Nanotube Films. *Science* **2004**, *305*,

1273–1276.

(35) Twedt, K. A.; Chen, L.; McClelland, J. J. Scanning Ion Microscopy with Low Energy Lithium Ions. *Ultramicroscopy* **2014**, *142*, 24–31.

(36) Knuffman, B.; Steele, A. V.; Orloff, J.; McClelland, J. J. Nanoscale Focused Ion Beam from Laser-Cooled Lithium Atoms. *New J. Phys.* **2011**, *13*, 103035–103044.

(37) Ziegler, J. James Ziegler - SRIM & TRIM http://www.srim.org/.

(38) Ferrari, A.; Robertson, J. Interpretation of Raman Spectra of Disordered and Amorphous Carbon. *Phys. Rev. B* **2000**, *61*, 14095–14107.

(39) Jorio, A.; Lucchese, M. M.; Stavale, F.; Achete, C. A. Raman Spectroscopy Study of Ar^+ Bombardment in Highly Oriented Pyrolytic Graphite. *Phys. Status Solidi* **2009**, *246*, 2689–2692.

(40) Martins Ferreira, E. H.; Moutinho, M. V. O.; Stavale, F.; Lucchese, M. M.; Capaz, R. B.; Achete, C. A.; Jorio, A. Evolution of the Raman Spectra from Single-, Few-, and Many-Layer Graphene with Increasing Disorder. *Phys. Rev. B - Condens. Matter Mater. Phys.* **2010**, *82*.

(41) Fantini, C.; Jorio, A.; Souza, M.; Strano, M.; Dresselhaus, M.; Pimenta, M. Optical Transition Energies for Carbon Nanotubes from Resonant Raman Spectroscopy: Environment and Temperature Effects. *Phys. Rev. Lett.* **2004**, *93*, 147406.

(42) Bruna, M.; Ott, A. K.; Ijäs, M.; Yoon, D.; Sassi, U.; Ferrari, A. C. Doping Dependence of the Raman Spectrum of Defected Graphene. *ACS Nano* **2014**, *8*, 7432–7441.

(43) Steiner, M.; Freitag, M.; Tsang, J. C.; Perebeinos, V.; Bol, A. A.; Failla, A. V.; Avouris, P. How Does the Substrate Affect the Raman and Excited State Spectra of a Carbon Nanotube? *Appl. Phys. A Mater. Sci. Process.* **2009**, *96*, 271–282.

(44) Duarte, A. S.; Rehbinder, J.; Correia, R. R. B.; Buckup, T.; Motzkus, M. Mapping Impurity of Single-Walled Carbon Nanotubes in Bulk Samples with Multiplex Coherent Anti-Stokes Raman Microscopy. *Nano Lett* **2013**, *13*, 697−702.

(45) Stobinski, L.; Lesiak, B.; Kövér, L.; Tóth, J.; Biniak, S.; Trykowski, G.; Judek, J. Multiwall Carbon Nanotubes Purification and Oxidation by Nitric Acid Studied by the FTIR and Electron Spectroscopy Methods. **2010**, *501*, 77–84.

(46) Pollard, A. J.; Brennan, B.; Stec, H.; Tyler, B. J.; Seah, M. P.; Gilmore, I. S.; Roy, D. Quantitative Characterization of Defect Size in Graphene Using Raman Spectroscopy. *Appl. Phys. lett* **2014**, *105*, 1–5.

(47) Tan, S.; Livengood, R.; Greenzweig, Y.; Drezner, Y.; Shima, D. Probe Current Distribution Characterization Technique for Focused Ion Beam. *J. Vac. Sci. Technol. B, Nanotechnol. Microelectron. Mater. Process. Meas. Phenom.* **2012**, *30*, 06F606.

(48) Myers, M. T.; Charnvanichborikarn, S.; Shao, L.; Kucheyev, S. O. Pulsed Ion Beam Measurement of the Time Constant of Dynamic Annealing in Si. *Phys. Rev. Lett.* **2012**, *109*, 2–5.

(49) Charnvanichborikarn, S.; Myers, M. T.; Shao, L.; Kucheyev, S. O. Pulsed Ion Beam Measurement of Defect Diffusion Lengths in Irradiated Solids. *J. Phys. Condens. Matter* **2013**, *25*.

(50) Kalbac, M.; Hsieh, Y.-P.; Farhat, H.; Kavan, L.; Hofmann, M.; Kong, J.; Dresselhaus, M. S. Defects in Individual Semiconducting Single Wall Carbon Nanotubes: Raman Spectroscopic and in Situ Raman Spectroelectrochemical Study. *Nano Lett.* **2010**, *10*, 4619–4626.

(51) Rossi, J. E.; Cress, C. D.; Merrill, A.; Soule, K. J.; Cox, N. D.; Landi, B. J. Intrinsic Diameter Dependent Degradation of Single-Wall Carbon Nanotubes from Ion Irradiation. *Carbon* **2015**, *81*, 488–496.

(52) Messenger, S. R.; Burke, E. A.; Summers, G. P.; Xapsos, M. A.; Walters, R. J.; Jackson, E. M.; Weaver, B. D. Nonionizing Energy Loss (NIEL) for Heavy Ions. *IEEE Trans. Nucl. Sci.* **1999**, *46*, 1595–1602.

(53) Lucchese, M. M.; Stavale, F.; Ferreira, E. H. M.; Vilani, C.; Moutinho, M. V. O.; Capaz, R. B.; Achete, C. A.; Jorio, A. Quantifying Ion-Induced Defects and Raman Relaxation Length in

Graphene. *Carbon* **2010**, *48*, 1592–1597.

TABLE OF CONTENT FIGURE